Long-Range Persistence of Femtosecond Modulations on Laser-Plasma-Accelerated Electron Beams

C. Lin,[1,2] J. van Tilborg,[1] K. Nakamura,[1] A. J. Gonsalves,[1] N. H. Matlis,[1] T. Sokollik,[1,3] S. Shiraishi,[1] J. Osterhoff,[1,*] C. Benedetti,[1] C. B. Schroeder,[1] Cs. Tóth,[1] E. Esarey,[1] and W. P. Leemans[1,3,†]

[1]*Lawrence Berkeley National Laboratory, Berkeley, California 94720, USA*

[2]*State Key Laboratory of Nuclear Physics and Technology, Peking University, Beijing, 100871, People's Republic of China*

[3]*University of California, Berkeley, California 94720, USA*

(Received 1 April 2011; published 1 March 2012)

Laser plasma accelerators have produced femtosecond electron bunches with a relative energy spread ranging from 100% to a few percent. Simulations indicate that the measured energy spread can be dominated by a correlated spread, with the slice spread significantly lower. Measurements of coherent optical transition radiation are presented for broad-energy-spread beams with laser-induced density and momentum modulations. The long-range (meter-scale) observation of coherent optical transition radiation indicates that the slice energy spread is below the percent level to preserve the modulations.

DOI: 10.1103/PhysRevLett.108.094801 PACS numbers: 41.75.Jv, 07.77.Ka, 41.60.Dk, 52.38.Kd

Laser plasma accelerators (LPAs) produce acceleration gradients on the order of tens to hundreds of GV/m, making them attractive as compact particle accelerators [1]. Over the past decade, significant progress has been made on LPAs, yielding quasimonoenergetic electron beams (e beams) with up to 1 GeV energy, a few percent integrated energy spread, and picocoulombs of charge [2]. Simulations and theory indicate that LPA e beams are of sufficiently short duration, high current, and low emittance to be candidates for drivers of tabletop free electron lasers [3], which have a broad range of applications. Critical to realizing these and other applications is a detailed knowledge of the properties of LPA e beams and, in particular, the slice energy spread (the energy spread at a longitudinal slice), which is desired to be below the percent level [4].

Slice energy spread measurements with femtosecond resolution have been outside the capability of available diagnostics. As will be demonstrated here, insight into the slice energy spread can be obtained by analyzing coherent optical transition radiation (COTR) of the e beam after long-range (meter-scale) evolution of laser-induced density modulations. The femtosecond LPA beam, which during acceleration typically resides within the first plasma oscillation, can overlap with a portion of the drive laser, resulting in momentum and density modulations [5–7]. While terahertz-based coherent transition radiation was used to measure bunch durations shorter than 50 fs [8,9], and an off-phase rf technique was used on >50-μm-period beam structure [10], to obtain evidence of submicron structure requires the use of optical-based diagnostics. Conventional free electron lasers routinely use COTR to monitor e-beam microbunching [11–14]. Recently, COTR was observed in LPA experiments [15,16].

For LPA beams, the observation has been that density modulations will disappear with propagation due to energy spread and divergence, and diagnostic foils were positioned at centimeter distances or less [15,16]. In this Letter, the presence and persistence of laser-induced optical-scale structures (density *and* momentum modulations) were studied by operating the LPA in a high-density regime ($\sim 10^{19}$ cm^{-3}), where the laser-electron overlap is enhanced (although resulting in a broad integrated electron energy spread). Images with clear evidence of COTR up to 3.8 m from the LPA source were observed, providing new insight into the slice electron energy spread and other LPA electron beam characteristics.

The experimental setup is shown in Fig. 1. The Lasers and Optical Accelerator Systems Integrated Studies laser system (wavelength ~800 nm) delivered 41-fs-duration (full width at half maximum [FWHM]) linearly polarized laser pulses with an on-target energy of 1.3 J. The pulse was focused by an off-axis parabolic mirror onto an underdense target (either a hydrogen-filled discharge capillary or a supersonic gas jet). The focused beam had a spot size of

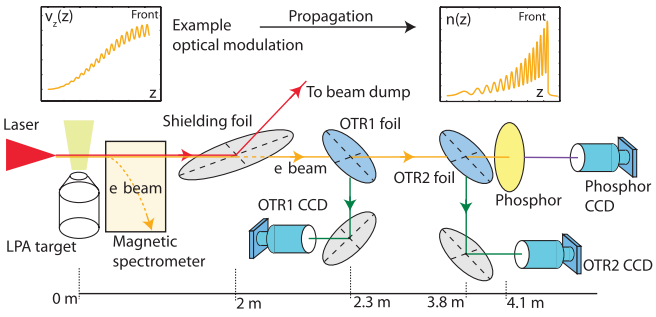

FIG. 1 (color). Schematic of the experimental setup for detection of OTR from the e beam propagating through two foils (OTR1 and OTR2), positioned several meters from the LPA source. The inset figures on the top illustrate how an example optical modulation on the longitudinal e-beam velocity distribution $v_z(z)$ can develop into a density modulation $n(z)$.

$w_0 = 23$ μm [with $I \sim \exp(-2r^2/w_0^2)$] and a Strehl ratio of $\simeq 0.85$, yielding a normalized vector potential of $a_0 \simeq 1.2$. The laser excited a plasma wave, in which plasma electrons were self-trapped and accelerated [1]. The energy spectrum of the accelerated electrons was characterized by a single-shot magnetic spectrometer [17]. The OTR measurements were taken subsequently with the electromagnet turned off. The remnant laser was separated from the e beam by 6-μm-thick Mylar and 14-μm-thick polycarbonate foils at 11° to the beam direction. Two additional 5-μm-thick aluminum-coated Mylar foils were placed 2.3 (OTR1 foil) and 3.8 m (OTR2 foil) downstream from the target, tilted by 45°. The first surface OTR emissions from both foils (peaked within a cone angle of γ^{-1} with respect to the direction of specular reflection, where γ is the relativistic Lorentz factor) were simultaneously recorded by 16-bit CCD cameras with 200 μm spatial resolution (FWHM). Both cameras (collection angle of 50 mrad) were imaging the foil surfaces, with a spectral sensitivity range of ~400–900 nm. At the end of the beam line (4.1 m from target), a calibrated phosphor screen [0.5-mm-thick lanex (fast front)] recorded the beam position and distribution [18].

The theoretical spatial distribution of OTR at an image plane was analyzed by Loos *et al.* [13]. It was shown that the incoherent contribution per unit bandwidth to the image is $dI_{\mathrm{Incoh}}(\mathbf{r})/dk = N \int d^2r' dz \rho(\mathbf{r}', z)|\mathbf{E}_s(\mathbf{r} - \mathbf{r}')|^2$ and the coherent contribution $dI_{\mathrm{Coh}}(\mathbf{r})/dk = N^2|\int d^2r' dz e^{ikz}\rho(\mathbf{r}', z)\mathbf{E}_s(\mathbf{r} - \mathbf{r}')|^2$, with $k = 2\pi/\lambda$ the wave vector, $\mathbf{r}$ the transverse coordinate, $\rho(\mathbf{r}, z)$ the normalized charge distribution, N the number of electrons, and $\mathbf{E}_s(\mathbf{r})$ the point spread function (~ 10 μm in size). These expressions were used to model the coherent enhancement (up to $\times N$ for full coherence) in peak photon counts. For beams much larger than the point spread function, it can be shown that the enhancement rapidly drops towards unity. Also, $I_{\mathrm{Incoh}}(\mathbf{r})$ scales with the transverse charge profile and $I_{\mathrm{Coh}}(\mathbf{r})$ with the transverse charge gradients. In summary, in order to observe COTR at (optical) wavelengths λ, significant transverse charge gradients *and* longitudinal charge substructure on a scale at (or below) λ are required.

The OTR emission was studied for various experimental conditions, by using gas jet and capillary targets. The accelerator was adjusted to produce beams that were stable over the measurement duration, ensuring applicability of an averaged electron energy spectrum. The expected number of OTR CCD counts in the absence of coherence was calculated for each shot, based on (i) the single-electron expression for incoherent OTR [19], (ii) the measured spatial charge profile, (iii) the averaged electron energy reference, and (iv) the calibrations and optical layout of the imaging system. The coherent enhancement was then defined as the ratio between the measured OTR CCD counts (integrated over the full image) to the expected incoherent counts. The measured standard deviation on the averaged electron energy reference resulted in an enhancement uncertainty indicated by the gray zone around unity in Fig. 2(a).

Figure 2 shows the observed OTR2 coherent enhancement as a function of e-beam charge (measured by the phosphor screen), taken in several experiments (see the legend). From each experiment, typical single-shot OTR and phosphor images were selected and shown in Figs. 2(b)–2(f), with decreasing coherent enhancement from top to bottom. Experiments IV and V provided a benchmark for the analysis procedure in the incoherent regime: The enhancement falls within the gray unitary zone where the OTR images are not only weak in counts but also match the transverse charge profile [see Figs. 2(e) and 2(f)]. For experiments such as I and II, the opposite is true: The integrated OTR counts are now over 2 orders of magnitude higher (with local enhancements up to ×1000), and the spatial structure no longer resembles the transverse charge profile.

Regimes of strong coherent enhancement are shown in Figs. 2(b) and 2(c), representing experiments I and II (see the legend) using a 0.9 mm (measured plasma FWHM length) gas jet target. The measured electron energy distribution followed an exponential distribution (temperature ~75 MeV) with a high-energy tail at ~125–250 MeV, which is typical [1] for continuous self-trapping at high densities above 10^{19} cm^{-3}. The OTR images contain "hot spots" several orders of magnitude higher in photon counts and $\gtrsim 200$ μm in size. This size is smaller than foil-scattering models predict and is potentially related to the complex correlated transverse and longitudinal momentum distribution. This will be the topic of future studies.

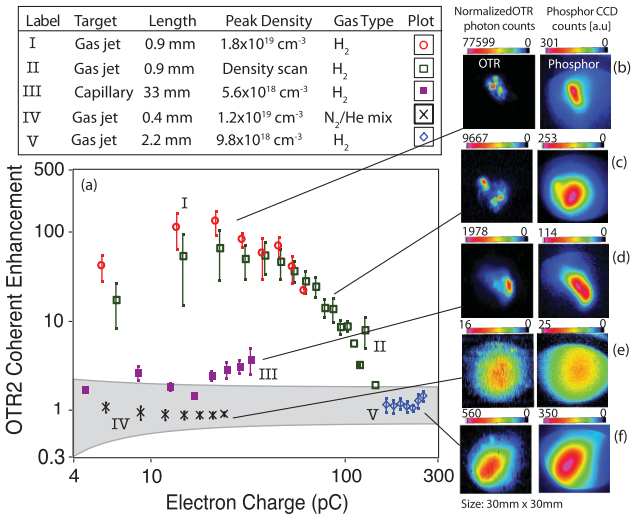

FIG. 2 (color). (a) The coherent enhancement at OTR2 as a function of charge with different targets. The experimental parameters are shown in the legend, with labels I–V. The error bars show the standard deviation. The gray area indicates the range where signals are considered to be incoherent. Typical OTR2 and phosphor images for each target are listed on the right of the plot, with decreasing coherent enhancement from shots (b)–(f).

Nevertheless, strong local enhancement from meter-scale-propagated LPA beams was observed.

Experiment II in Fig. 2(a) displays the enhancement in a density scan from 1.7×10^{19} to 2.3×10^{19} cm^{-3}. At the higher densities, the number of accelerated electrons increases due to the lower trapping threshold. However, the beam quality (e.g., the slice energy spread) deteriorates due to dephasing and beam loading effects, reducing the density modulation at the OTR screen. For electron charges in the range of 20–80 pC, the modulation has persisted. The phosphor images were not observed to be elliptical along the polarization axis (as observed by Mangles *et al.* [5]). This is possibly explained by only part of the e beam being affected by the laser and the laser-driven divergence being smaller than the intrinsic divergence. At lower plasma densities where even less charge is injected, a longer plasma wave is formed ($\lambda_p \propto n_e^{-1/2}$) which reduces the overlap between electrons and laser and limits the modulation amplitude and coherent enhancement. This was confirmed for the low-charge shots for experiments I and II in Fig. 2 but also for the capillary experiments III, where the density was even further reduced [see also Fig. 2(d)]. The latter experiment was performed with a 33-mm-long electrically discharged capillary of 250 μm diameter [2], with an electron energy distribution resembling a Gaussian distribution centered at ~210 MeV and a width (FWHM) of ~190 MeV.

In experiment IV [400-μm-long gas jet, electron energy distribution a Gaussian distribution centered at ~45 MeV with width (FWHM) ~40 MeV], gas of a 1%-nitrogen 99%-helium mixture was used. Nitrogen electrons were tunnel-ionized by the laser and injected into the plasma wave with additional transverse momentum (larger divergence) in the laser polarization direction [20]. This led to larger beams at the OTR foils and smaller transverse charge gradients such that the conditions for coherent enhancement were no longer met. For experiment V (2.2-mm-long gas jet, exponential energy distribution at effective temperature ~120 MeV), in addition to the larger divergences observed, also the enhanced charge (> 100 pC) played a role in smoothing out microstructures.

To provide insight into the experimental observations, a model has been developed that can elucidate how a density modulation can develop at larger propagation distances. For simplicity, it relies on radial symmetry and is solely based on a correlated longitudinal momentum modulation. Consider an initial velocity and density distribution for those electrons contributing to the coherent enhancement, defined as

$$f_0(z,\beta_z,\beta_r) = \frac{\exp[-\frac{z^2}{2\sigma_z^2}]}{\sqrt{2\pi}\sigma_z}\frac{\exp[-\frac{(\beta_z-\bar{\beta}_z)^2}{2\sigma_{\beta_z}^2}]}{\sqrt{2\pi}\sigma_{\beta_z}}\frac{\exp[-\frac{\beta_r^2}{2\sigma_{\beta_r}^2}]}{2\pi\sigma_{\beta_r}^2}, \quad (1)$$

with $\bar{\beta}_z = \sqrt{\beta_0^2 - \beta_r^2} - \delta_L \sin k_m z$, $\beta_0 = \sqrt{1-\gamma^{-2}}$, and δ_L the amplitude of the longitudinal momentum modulation at period k_m. Also, σ_z is the bunch duration, σ_{β_r} the divergence, and σ_{β_z} the slice energy spread ($\Delta\gamma/\gamma = \sigma_{\beta_z}\gamma^2$). The electrons are initially transversely confined to $r = 0$. At later time t (corresponding to a propagation distance $L = tc$), the ballistic motion has modified the longitudinal and transverse charge distribution to $\rho(r,z) = \int dz' f_0(z', \frac{z-z'}{L}, \frac{r}{L})$. A numerical integration allows for study of the dynamic $\rho(r,z)$ and its corresponding OTR image $I_{\mathrm{Incoh}}(\mathbf{r}) + I_{\mathrm{Coh}}(\mathbf{r})$.

The observations in experiment I show enhancements in peak counts at the coherent spots of more than ×1000. By using the measured LPA parameters, an upper bound for the slice energy spread $\Delta\gamma/\gamma$ can be derived based on the model of Eq. (1). The values of β_z used in the calculations match the experimentally measured range (0–250 MeV). The modulation wavelength was set at $\lambda = 800$ nm. First, a longitudinal Gaussian e beam of length $\sigma_z = 2$ μm ($\sigma_z \simeq \lambda_p/2$) was estimated [1]. Second, it was assumed that, for those shots where the strongest coherence was observed, the modulation strength δ_L was such ($\delta_L \simeq 6 \times 10^{-8}$) as to yield optimized density modulations at $L = 3.8$ m [see the inset in Fig. 3(b)]. Third, the widths of the measured coherent spots were of the order of ≃ 150–300 μm (rms), hence the choice of parameter $\sigma_{\beta_r} = 40$ μrad as a conservative lower limit. A charge of 5 pC ($N = 3.1 \times 10^7$ electrons) for the coherence-contributing part of the e beam was used. The spectral integration was performed over 400–900 nm. Figure 3 shows the modeled coherent enhancement for a range of electron energies and slice energy spreads. It is evident that only the high-energy electrons with low energy spread contribute to enhancement. Considering that ≲ 10% of the measured electron energy distribution in experiment I extends beyond $\gamma = 250$ (125 MeV), the 5 pC of charge used for the calculation represents a conservative upper limit. Consistency with the observations suggests a slice

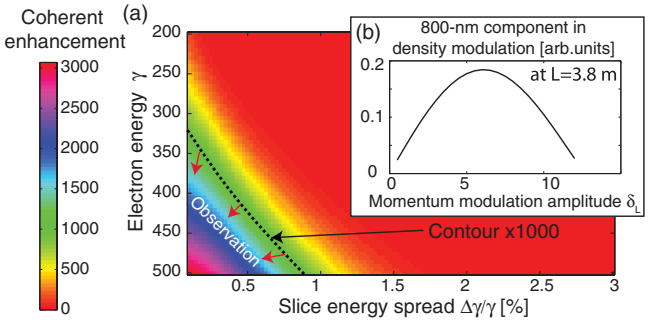

FIG. 3 (color). (a) Modeled coherent enhancement as a function of electron energy and slice energy spread (see the text for an explanation of the parameters used). The experimental observations (× 1000 enhancement) suggest that the coherence is attributed to high-energy electrons ($\gamma \gtrsim 300$) with a slice energy spread ≲ 1%. Inset (b) shows the 800-nm spectral component of the on-axis longitudinal density modulation $|\int dz \rho(0,z) e^{ik_m z}|$ as a function of δ_L (by using $L_0 = 3.8$ m, $\gamma = 500$, and $\Delta\gamma/\gamma = 0.5\%$).

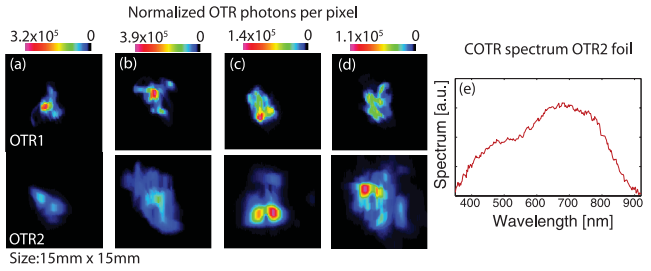

FIG. 4 (color). (a)–(d) Comparison of the simultaneously measured single-shot OTR1 and OTR2 images in the 0.9 mm gas jet experiment III. The color scale represents the calibrated photon counts. Note that in images (c) and (d) the OTR2 foil, while farther from the source, emits more COTR than the OTR1 foil. (e) One of several shots where the optical spectrum was measured (few-nanometer spectral resolution).

energy spread $\Delta\gamma/\gamma \lesssim 0.5\%$ for those electrons contributing to the coherence. It is important to mention that it is likely that (i) there is less charge in the high-energy tail, (ii) a longer bunch at the 3.8-m foil, (iii) a larger divergence of the coherence-contributing electrons, and/or (iv) a non-optimized modulation strength δ_L for density modulations at $L = 3.8$ m, which all reduce the modeled coherent enhancement and hence yield an even smaller slice energy spread in order to explain the observations.

In addition to a small slice energy spread, a finite propagation length L is also necessary for microstructure development. As predicted in the model, this allows for a scenario where an OTR screen located farther away would emit more coherent radiation than a screen closer to the source. To verify this concept experimentally, OTR1 and OTR2 images were simultaneously recorded during experiment I [see Fig. 2(a)]. Figures 4(a)–4(d) are four correlated single-shot OTR1 and OTR2 images. In Figs. 4(a) and 4(b), the peak intensity of OTR1 is about 10 times higher than OTR2, consistent with divergence and energy spread reducing the microstructure over longer propagation. Such behavior is observed for over 90% of the shots. However, for about 10% of the shots, the peak intensity of OTR2 is on the same level or higher than OTR1 [see Figs. 4(c) and 4(d)], consistent with relativistic bunching from a correlated momentum modulation.

In an experiment similar to III, a transmission grating (300 lines/mm) was placed in front of the OTR2 CCD; see Fig. 1. The camera now imaged the capillary exit. The small e-beam source size and the narrow OTR cone angles allowed for few-nanometer resolution at optimum COTR collection. Only a few optical spectra were above background with an example spectrum shown in Fig. 4(e) (corrected for grating and CCD spectral sensitivity). The broad spectrum indicates that the laser pulse induced electron modulations over the full optical spectral range 400–900 nm (as also observed by Glinec *et al.* [15]), consistent with strong red- and blueshifting of the drive laser as measured with an optical spectrometer on the transmitted laser. While Fig. 3 assumed $\lambda = 800$ nm, shorter e-beam microstructure would require an even smaller slice energy spread to explain the observations.

In conclusion, enhancement in OTR in excess of 3 orders of magnitude over the incoherent level was observed from broad-energy-spread LPA e beams at up to 4 meters from the LPA exit, indicating long-range persistence of femtosecond e-beam structure. Observed fluctuations in relative coherent enhancement between two OTR stations are consistent with dynamic changes of the bunch structure due to beam velocity bunching. These observations imply that, for those electrons participating in the coherent emission, the slice energy spread is $\lesssim 0.5\%$-level. The measurements have provided new insight into the LPA beam characteristics with important implications for the realization of a LPA driven free electron laser, which requires a low energy spread over a free electron laser cooperation length.

The authors thank C. G. R. Geddes, M. Chen, A. Lumpkin, D. Syversrud, Z. Eisentraut, and N. Ybarrolaza, and C. L. also thanks Professor Z. Guo for his guidance. This work was supported by the U.S. Department of Energy under Contract No. DE-AC02-05CH11231, DTRA under Contract No. WF006631B, the National Science Foundation under Grants No. PHY-0935197 and No. PHY-0917687, and the China Scholarship Council.

*Present address: DESY, Hamburg, Germany.
†WPLeemans@lbl.gov

[1] E. Esarey, C. B. Schroeder, and W. P. Leemans, Rev. Mod. Phys. **81**, 1229 (2009).
[2] W. P. Leemans *et al.*, Nature Phys. **2**, 696 (2006).
[3] F. Grüner *et al.*, Appl. Phys. B **86**, 431 (2007).
[4] Z. Huang and K.-J. Kim, Phys. Rev. ST Accel. Beams **10**, 034801 (2007).
[5] S. P. D. Mangles *et al.*, Phys. Rev. Lett. **96**, 215001 (2006).
[6] K. Németh *et al.*, Phys. Rev. Lett. **100**, 095002 (2008).
[7] A. H. Lumpkin *et al.*, in *Proceedings of FEL 2007, Novosibirsk, Russia* (JACoW, http://www.jacow.org, 2007), p. 294.
[8] J. van Tilborg *et al.*, Phys. Rev. Lett. **96**, 014801 (2006).
[9] A. D. Debus *et al.*, Phys. Rev. Lett. **104**, 084802 (2010).
[10] K. N. Ricci and T. I. Smith, Phys. Rev. ST Accel. Beams **3**, 032801 (2000).
[11] A. H. Lumpkin *et al.*, Phys. Rev. Lett. **88**, 234801 (2002).
[12] P. Salén *et al.*, in *Proceedings of FEL 2009, Liverpool, UK* (JACoW, http://www.jacow.org, 2009), p. 739.
[13] H. Loos *et al.*, in *Proceedings of FEL 2008, Gyeongju, Korea* (JACoW, http://www.jacow.org, 2008), p. 485.
[14] A. H. Lumpkin *et al.*, Phys. Rev. ST Accel. Beams **12**, 080702 (2009).
[15] Y. Glinec *et al.*, Phys. Rev. Lett. **98**, 194801 (2007).
[16] O. Lundh *et al.*, Nature Phys. **7**, 219 (2011).
[17] K. Nakamura *et al.*, Rev. Sci. Instrum. **79**, 053301 (2008).
[18] K. Nakamura *et al.*, Phys. Rev. ST Accel. Beams **14**, 062801 (2011).
[19] C. B. Schroeder *et al.*, Phys. Rev. E **69**, 016501 (2004).
[20] A. Pak *et al.*, Phys. Rev. Lett. **104**, 025003 (2010).